# Tunable Dynamic Walking via Soft Twisted Beam Vibration

Yuhao Jiang<sup>1</sup>, Fuchen Chen<sup>2</sup>, and Daniel M. Aukes<sup>2</sup>

Abstract—We propose a novel mechanism that propagates vibration through soft twisted beams, taking advantage of dynamically-coupled anisotropic stiffness to simplify the actuation of walking robots. Using dynamic simulation and experimental approaches, we show that the coupled stiffness of twisted beams with terrain contact can be controlled to generate a variety of complex trajectories by changing the frequency of the input signal. This work reveals how ground contact influences the system's dynamic behavior, supporting the design of walking robots inspired by this phenomenon. We also show that the proposed twisted beam produces a tunable walking gait from a single vibrational input.

Index Terms—Soft Sensors and Actuators; Soft Robot Materials and Design; Modeling, Control, and Learning for Soft Robots

#### I. Introduction

CTUATION and its transmission through soft robotic systems have driven extensive study in recent decades [1], [2], [3]. Unlike actuation in traditional rigid-body robotic systems – which relies on motors, gears, shafts, and belts to actuate and transmit power – the morphology of soft actuators can be deformed to subsequently alter body shapes and drive robots by stimulating or deforming soft materials. While numerous soft actuators have been developed to drive soft robots in applications like human-robot interaction, bioinspired robots, and wearable robotic systems, the power of these systems is usually low and actuators are usually bulky. Moreover, due to the non-linearity of hyper-elastic materials and the complexity of powered soft systems, dynamic modeling is challenging and thus can be underutilized during design.

In this paper, we propose a novel actuating method for walking robots using the coupled compliance of soft twisted beams with ground contact. This mechanism transforms simple, periodic inputs into complex cyclic motion under contact with the ground. More specifically, we show how this phenomenon can be adopted to generate tunable bidirectional walking via

Manuscript received: October 23, 2022; Revised January 8, 2023; Accepted February 3, 2023.

This paper was recommended for publication by Editor Cecilia Laschi upon evaluation of the Associate Editor and Reviewers' comments.

This material is based upon work supported by the National Science Foundation under Grant No. 1935324. (Corresponding author: Daniel Aukes)

<sup>1</sup>Yuhao Jiang is with School for Engineering of Matter, Transport and Energy, Fulton Schools of Engineering, Arizona State University, Tempe, AZ, 85281, USA yuhao92@asu.edu

<sup>2</sup>Fuchen Chen and Daniel Aukes are with School of Manufacturing Systems and Networks, Fulton Schools of Engineering, Arizona State University, Mesa, AZ, 85212, USA fchen65@asu.edu; danaukes@asu.edu

Digital Object Identifier (DOI): see top of this page.

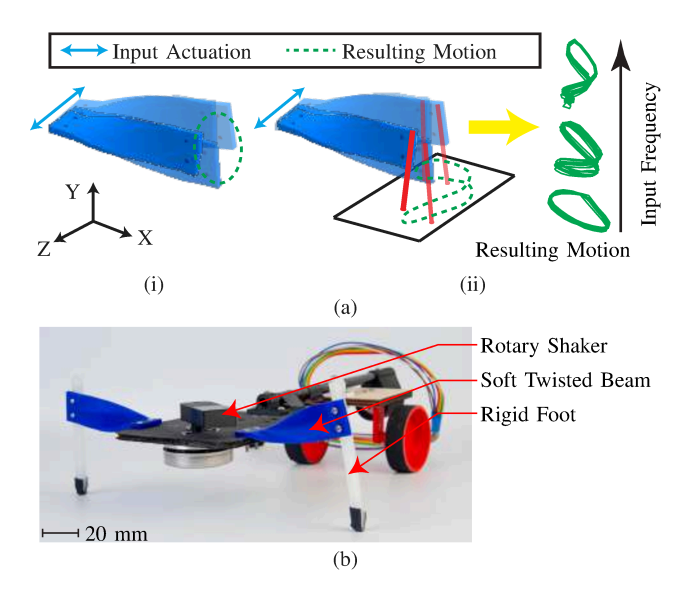


Fig. 1. Concept demonstration and beam design. (a): Conceptual demonstration of the operation principle: (i) without terrain contact; (ii) with terrain contact. (b): Walking robot prototype.

the input frequency. This study fits under the umbrella of a new class of devices we call "Soft, Curved, Reconfigurable, Anisotropic Mechanisms" (SCRAMs), which we have previously studied in the context of pinched tubes[4], [5], [6], and buckling beams[7], [8]. By taking advantage of the shape and material properties in soft structures, complex actuation signals for generating complex motion can be consolidated and simplified.

Fig. 1(a) demonstrates the proposed concept. In (i), a soft, twisted beam under a linear vibratory input (shown by the blue arrow) generates a repeating, semicircular trajectory at the tip (shown in dashed green lines). With terrain contact, this motion results in a more complex motion that can be controlled and further adapted for robot walking (ii) using the prototype as shown in Fig. 1(b).

The rest of the paper is organized as follows. Sec. I-A discusses related prior work; Sec. I-B summarizes this paper's contributions. Sec. III describes the beam prototyping. Sec. II discusses how beam motion behaves under various excitation frequencies with an FEA model, as well as how the output changes as a function of twist angle. We then propose a simplified model in Sec. II-B for exploring the system at reduced computational cost and similar performance. Sec. IV discusses the experimental validation of our concept with a walking robot prototype in Sec. IV-B. Results and current

limitations are discussed in Sec. V along with a discussion of planned future work in Sec. VI.

#### A. Background

Helical shapes, twisted surfaces, and chirality are found throughout the natural world, such as the DNA molecule [9], various seeds [10], [11], and human sperm [12]. These natural phenomena have aroused a series of theoretical studies regarding the self-assembly and transition of complex helical strands such as cables, ropes, and ribbons [13], [14], [15]. Inspired by nature and the mathematical properties of anisotropic, curved, chiral, and helical shapes, scientists have developed soft systems that can generate complex asymmetric motion for use in actuation [16], [17] and sensing [18], [19]. Various methods have been proposed to utilize the stiffness and the geometry change of continuous curved surfaces for locomotion [20], [21], [4], [5]. Twisting mechanisms have also been applied in the actuation of robotic fingers [22] and twisting tube actuators [23]. Zhao et al. [24] developed a twisting ribbon robot that can roll and maneuver in unstructured environments. The above work demonstrates that curved geometry can play a role in tuned dynamic gaits in soft and flexible robotic systems. The large deflection effects and its dynamic application in origami and foldable miniature walking robots have also been studied [25], [26], [27]. Maruo et al. [28] propose a similar mechanism using structural anisotropy and cyclic vibration to create complex motion for manipulation. Our paper, conversely, studies how soft, twisted beams interacting with the ground can generate complex walking locomotion via simple vibratory input.

Though electric motors are most often used to actuate legged robots[29], the mass and size constraints of centimeter and millimeter-scale robots has also led researchers to investigate pneumatic [30], tendon-based [31], and piezoelectric actuation strategies [32], [33]. In contrast to these approaches, the coupled compliance of the soft twisted beams can be used to directly generate complex, tunable walking patterns that typically require coordinated control signals to multiple actuators. This is the same principle behind bristlebots – a well-studied and simple class of walking mechanisms – which use oriented bristles and vibration-based actuation to move forward [34]. This has also resulted in bristlebot-inspired walking micro-robots [35].

While the above research demonstrates the capacity for vibration-based actuation to drive terrestrial robots, the type of motions observed in these systems is limited due to the direct connection to the input actuator. This has artificially limited applications to simpler tasks on lower-complexity terrains. In contrast, we propose mechanisms for establishing more complex leg dynamics using soft and compliant twisted beams in this paper, which can be tuned via the geometric, inertial, and material design parameters and used to simplify the control signals typically associated with multi-DOF walking robots.

#### B. Contributions

The contributions of this paper may be summarized as follows: 1) A new mechanism has been proposed for generating

walking locomotion using soft twisted beams under interaction with the ground; 2) A new computationally-efficient pseudorigid body (PRB) model has been developed that accurately describes the dynamic behavior of the highly nonlinear system. We then 3) demonstrate how walking direction and speed can be tuned by the frequency of the input actuator both experimentally and in simulation.

#### II. SYSTEM MODELING

We conduct a series of FEA-based dynamic simulations with PyChrono [36], demonstrating how input frequency, beam chirality, and the magnitude of beam twist angle alter the dynamic motion of the beam. A simplified pseudo-rigid-body (PRB) model is then proposed and evaluated for improving simulation speed in the presence of contact.

### A. Dynamic modeling using FEA approach

**FEA model setup:** We developed a FEM-based dynamic model, which consists of a 120-element mesh generated from a single layer of 6-field Reissner-Mindlin shells, seen in Fig. 2(a). The mesh geometry replicates the beam design outlined in Sec. III; the material properties for TPU came from its datasheet

The input actuator shakes the proximal end of the beam along the z-axis as shown in Fig. 2(a). The input signal is

$$x = A\sin(2\pi ft),\tag{1}$$

where x is the actuation travel position with the unit of mm, f is the rotating frequency of the motor in Hz and A is the amplitude in mm with  $A=2\,\mathrm{mm}$ .

Input frequency V.S. resulting motion: The coupled stiffness of twisted beams can be exploited by exciting it at specific frequencies to create highly differentiated motion. To demonstrate this effect, we swept the input frequency from  $f=1\,\mathrm{Hz}$  to  $f=45\,\mathrm{Hz}$  in 1 Hz increments. The trajectory of the beam's distal end was recorded throughout the simulation and is shown in Fig. 2(d). While the resulting trajectory is in three dimensions, the Y-Z plane motion is observed to dominate the resulting behavior. Thus Y-Z plane trajectories were demonstrated throughout the paper. As can be seen, the beam's trajectory varies significantly in shape and size as a function of input frequency. At certain input frequencies such as  $9\,\mathrm{Hz}$ ,  $17\,\mathrm{Hz}$ ,  $25\,\mathrm{Hz}$ , the trajectory exhibits an ovallike shape, whereas at frequencies such as  $1\,\mathrm{Hz}$  and  $41\,\mathrm{Hz}$  the trajectory appears more linear.

Beam twist V.S. resulting trajectory: A beam's magnitude of twist plays an important role in the generation of elliptical motion, while its chirality (twist direction) can be used to mirror the patterns observed at different magnitudes. We explored the relationship between beam twist angle  $\phi$  and its resulting trajectory through a pair of studies. In the first study, we modeled a series of beams with identical dimensions but a range of twist angles from  $\phi = 0^{\circ}$  to  $\phi = 180^{\circ}$  with a step of  $5^{\circ}$ . The input amplitude and frequency was held constant at  $f = 15\,\mathrm{Hz}$  and  $A = 2\,\mathrm{mm}$ . The distal end's trajectory was recorded during the simulation; the selected result is shown in Fig. 2(e). As the twist angle  $\phi$  increases,

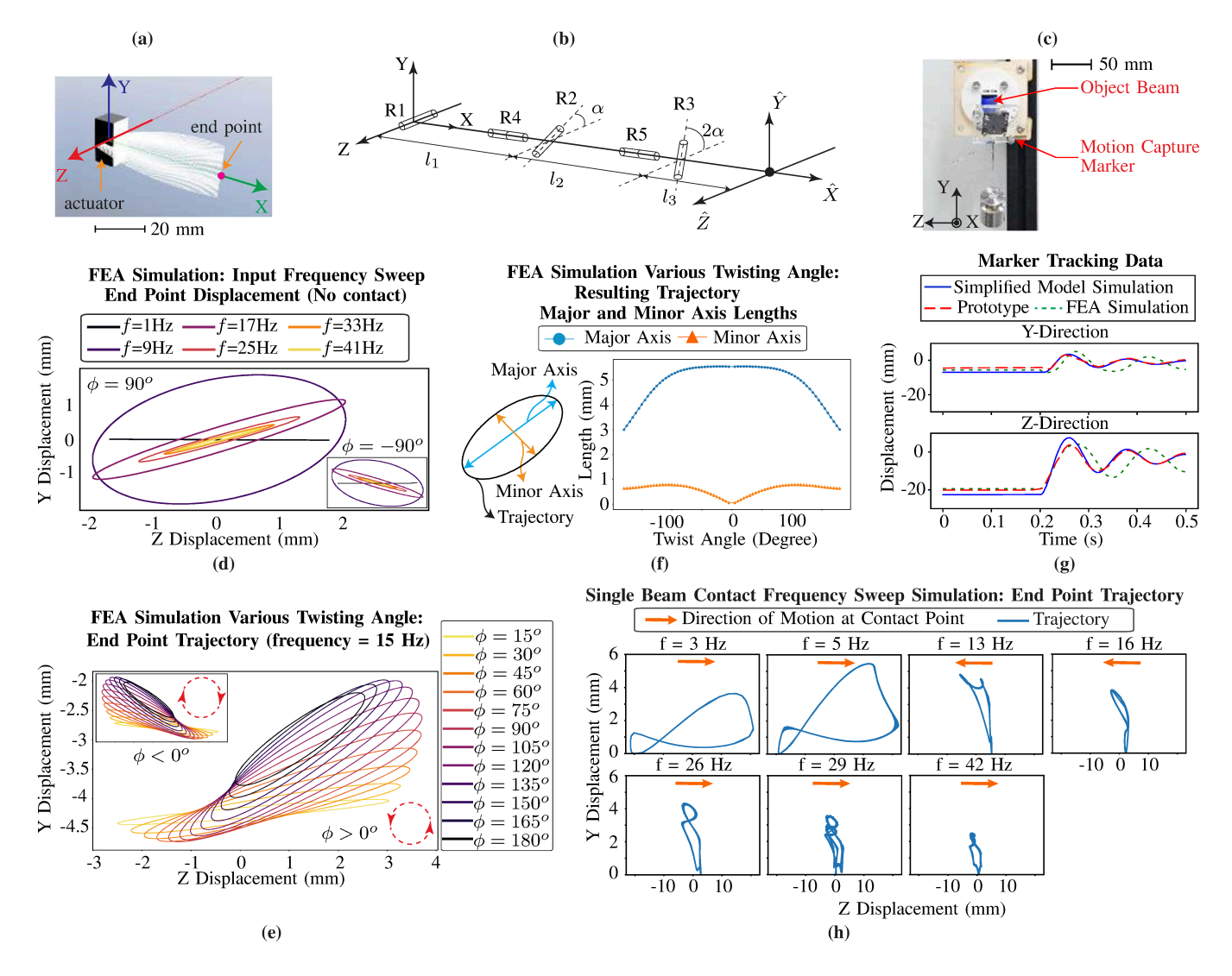


Fig. 2. **Results from FEA simulations.** (a): Beam FEA mesh model; (b): The proposed analytical model; (c): The lab test setup for simplified model fitting; (d): Beam end point trajectory results from frequency sweep simulation using FEA simulation; (e): Beam end point trajectory results from FEA simulation with twist angle from  $\phi = -180^{\circ}$  to  $\phi = 180^{\circ}$ ; (f): Major and minor axis lengths of beam end point trajectory with respect to twist angle  $\phi$ ; (g): Example marker tracking data from calibration experiments; (h): Beam end point trajectory results from frequency sweep simulation with contact using the proposed analytical model;

the output trajectory's orthogonal motion (along the Y axis) grows. To better understand the nature of the shapes generated, we approximated each trajectory as an elliptical path using a least squares minimization function [37], identified the major and minor axes of the approximate ellipses at each frequency, and then measured their length. The results, shown in Fig. 2(f), highlight how twist magnitude and the resulting coupling of stiffness play a role in the evolution of elliptical paths in twisted beams. Based on this result, the twist angle  $\phi$  of the prototype beams is set as  $\phi = 90^\circ$  and  $\phi = -90^\circ$  for the more distinguished spans in both major and minor axis.

In the second set of simulations, we compared beams of equal magnitude but opposite direction  $(\phi_1 = -\phi_2)$ . As seen in Fig. 2(e), beams of equal magnitude but opposite chirality result in trajectories mirrored across the Y-axis, the beams' axis of symmetry (path shape and direction of motion, as highlighted in Fig. 2(e) by the red dashed arrows).

#### B. Pseudo-rigid-body modeling

While the FEA simulation qualitatively validates the proposed concept, its shortcomings have limited its further use. First, accurate FEA simulation relies on well-defined meshes and models that precisely describe the stiffness and damping of materials. Prototyping with 3D printing introduces variation within the beam and between different beams, with highly viscoelastic soft materials, resulting in a poor fit from our FEA model. To address this, the FEA simulation must be calibrated to each prototype - a computationally expensive endeavor. Considering our use-case for terrestrial simulation, the addition of contact makes FEA models even less feasible. Hence, in order to simulate faster while accurately exploring the dynamic system's behavior with contact, a simplified model using the pseudo-rigid-body (PRB) model is then proposed to describe the dynamic behavior of twisted beams over time. The principal differences between this approach and the FEA model are that, by reducing the number of degrees of freedom (DOF) through a set of principled assumptions about deformation, a more computationally efficient PRB representation can be used within off-the-shelf rigid body simulators, which solve problems of contact and friction more efficiently, allowing us to more thoroughly explore the system-level dynamics of the walking robot. An evolutionary-optimization-based fitting process can then be more easily applied to quickly fit the model to each prototype's captured properties, allowing us to simulate system motion with higher accuracy.

Pseudo-rigid-body model setup: Off-diagonal coupling parameters, along with hyper-elastic material models, make the dynamics of twisted soft systems more complex than classical approaches such as Euler-Bernoulli models can approximate. Fundamental research has analyzed the behavior of pre-twisted beams using variational formulations [38] and geometrically intrinsic dynamic models [39], for the dynamics of stiff, pre-twisted beams. Banerjee demonstrates the use of approximate representations of twisted beam dynamics using simplified models with two cooperative linear motions across two mutually-orthogonal planes [40]. Other work by Howell also demonstrates the suitability of cantilever-style PRB models for large deflections [41], [42]. Due to this prior art, the PRB model with revolute springs attached to a number of joints subdividing the beam was selected to describe the two-DOF orbit at the beam's distal end. The design parameters, stiffness, and damping values were then calibrated to match the manufactured prototype's behavior. Although the kinematics are specifically selected for analyzing the dynamic behaviors observed in our system, making it less general, the computational cost savings over more general approaches permitted more and better fitting to our prototype and enabled more parameter exploration.

We use a linear spring-damper model of the form  $\tau = k\theta + b\dot{\theta}$  to describe the moments about each joint, where  $\tau$ represents the torque about each joint, k represents the linear spring constant in bending, b represents linear joint damping, and  $\theta, \theta$  represent the local rotation and rotational velocity, respectively, of each joint from its unloaded, natural shape. Since the cross-sectional area of each beam is constant along its axial length, the spring stiffness constant k represents a distributed bending stiffness about three revolute joints – R1, R2, and R3 – which are distributed perpendicularly along the beam's axial direction, as seen in the complete model in Figure. 2(b). Two additional revolute joints – R4, and R5 – are aligned with the beam's local axial direction and capture the twist of the beam, represented by  $\phi$ . The same springdamper model is also applied to represent the twisting stiffness between these two joints.

Together, these joints exhibit the same coupled stiffness of twisted beams observed in experiments. Based on the results from [41], [42], the location of joints in a compliant, cantilever-style PRB model under large deflections should not be evenly distributed along the beam; we thus parameterize  $l_1$ ,  $l_2$ ,  $l_3$  as the distances between R1-R2, R2-R3, and R3 - distal end, respectively. The total length of the beam,  $l = l_1 + l_2 + l_3 = 50$  mm, is identical to the prototype. Mass is evenly distributed using  $\rho = 1210kg/m^3$  (the density of

TPU), with an assumption of constant cross-sectional area. The sum of all links' mass is equal to the prototypes' mass of  $m=5.17\,\mathrm{g}$ .

**Model fitting:** A set of dynamic experiments was conducted to obtain the motion of the end of the beam when released from an initial deformed state. The test setup can be seen in Fig. 2(c). At the beginning of the test, the beam was deformed with a 200 g load applied to the end. The load was instantaneously released from the beam while the position of the beam's tip was recorded as the beam returned to rest at its natural unloaded position. Three optical tracking markers were attached to the end of the beam to obtain the tip's motion. After the data was recorded, a differential evolution optimizer [43] was implemented to fit the model variables  $(k, b, l_1, l_2, l_3)$  by minimizing the averaged error between simulation marker position data  $(M_i)$  and the reference data from experiments  $(\hat{M}_i)$  and objective function

$$Min \left\{ \sqrt{\sum_{j=0}^{n} \sum_{i=1}^{3} \left[ (M_i(j) - \hat{M}_i(j))^2 \right] / (3n)} \right\}.$$
 (2)

The optimization variable set is defined by  $(k, b, l_1, l_2, l_3)$ , where  $l_3 = 50 - l_1 - l_2$ . In this fitting progress, the proposed model was simulated in MuJoCo [44] and Python. We observed that  $l_1$  tended to converge at the minimum bound of 1 mm; We therefore simplified the model by setting  $l_1 = 0$ , which yields the variable set as  $(k, b, l_2, l_3)$ , where  $l_3 = 50 - l_2$ . The optimizer finally converged with an averaged dynamic tracking error of 9.38%, where  $k = 0.340 \, \text{N·m/rad}$ ,  $b = 0.0029 \, \text{N·m/(rad/s)}$ ,  $l_2 = 23.66 \, \text{mm}$ ,  $l_3 = 26.34 \, \text{mm}$ .

To compare the two models with the prototype, we conducted the FEA simulation using the same test setup as shown in Fig. 2(c). The marker tracking data from the test is shown in Fig. 2(g). As can be seen, the proposed simplified model with calibration outperforms the FEA model on tracking the dynamic motion of the twisted beam prototype. The averaged dynamic tracking error using the simplified model is 9.38%, and 34.79% using the uncalibrated FEA model. The average time cost for a 10 s simulation with an Intel i9-7900K CPU and 32GB RAM was also shortened from 82.5 s with the FEA model to 1.2 s using the PRB model.

Simulation of single beam vibration with contact: Using the newly proposed PRB model, we conducted a series of beam vibration simulations with contact in MuJoCo. The test setup is identical to that described in Sec. IV-A. During the simulation, the slider is actuated to sweep from  $f=1\,\mathrm{Hz}$  to  $f=45\,\mathrm{Hz}$  using (1) with amplitude  $A=2\,\mathrm{mm}$  while the beam's endpoint position is recorded. The resulting trajectory and the direction of motion at the contact point are shown in Fig. 2(h). As can be seen, the resulting motion differs from the free vibrating beam due to contact with the floor. A figure '8' loop is observed at the input frequency  $f=16\,\mathrm{Hz}$  and  $f=26\,\mathrm{Hz}$ . Moreover, the direction of motion at the contact point, as indicated by orange arrows, also alters as a function of the input frequency.

# III. Design and manufacturing of the prototype $$\operatorname{\mathtt{BEAM}}$$

We designed and manufactured a series of prototypes to validate the proposed concept. 3D printing was selected to reduce manufacturing time and to permit a broad design space. Because hard printable plastics must be printed with very thin geometries and at higher precision to achieve the desired range of leg stiffnesses, we selected soft printable materials that could be printed at millimeter to centimeter scales, more than 30 layers thick, while achieving the desired range of leg stiffness in all dimensions, in order to ensure a wide design space. We compared two commercial soft filaments: thermoplastic elastomer (TPE)<sup>1</sup> with a Shore hardness of 92A, and thermoplastic polyurethane (TPU)<sup>2</sup> with a Shore hardness of 95A. The Young's modulus of the TPE is reported as 7.8 MPa in the datasheet, whereas the Young's modulus of the TPU is reported as 26 MPa. Although the difference in the hardness between the two materials is relatively small, the TPU 95A 's higher stiffness supports our target payload and deflects less at the same dimensions compared to the TPE, while demonstrating the dynamic behavior desired for terrestrial locomotion. Thus, we selected the TPU 95A as the prototyping material.

Based on the results from Sec. II-A, a number of prototypes with  $\phi=90^\circ$  and  $\phi=-90^\circ$  were manufactured with all other design parameters held constant, as shown in Fig. 3(b). The beam is right-handed chiral if  $\phi>0$  and left-handed if  $\phi<0$ . The design diagram is shown in Fig. 3(a); design parameters can be found in Table I.

TABLE I DESIGN PARAMETERS

| Parameter                  | Symbol   | Value | Unit             |
|----------------------------|----------|-------|------------------|
| Beam length                | l        | 50    | mm               |
| Beam width                 | w        | 20    | mm               |
| Beam thickness             | t        | 3     | mm               |
| Beam total twist angle     | $\phi$   | 90    | degree           |
| Beam segmental twist angle | $\alpha$ | 45    | degree<br>degree |

#### IV. PROTOTYPE TESTS

The results of our experiments demonstrate how vibrating, twisted beams with terrain interactions exhibit similar behavior in real life to model-based results.

#### A. Single Beam Contact Test

This experiment demonstrates how the output trajectory and its orientation can be influenced by the input signal driving frequency in the presence of highly nonlinear ground interactions. This section demonstrates a relatively constrained, prescribed experiment, whereas the next section demonstrates the same phenomonon observed in a less prescribed manner with a free-walking platform.

The test setup in Fig. 3(c) and (d) shows a linear stage whose oscillating, forward-backward motion is dictated by the

rotating crank of a brushless motor<sup>3</sup>. The motor is controlled by an ODrive<sup>4</sup> motor control board. We again use (1) to control the speed of the motor, with A = 2 mm, and  $f = \{1-40\}$  Hz. The beam is mounted to the linear stage and optical tracking markers are mounted to the proximal and distal ends of the beam. An OptiTrack Prime 17W optical motion tracking system is then used to track the position of the system at a rate of 360 Hz. A plate with four load cells mounted perpendicularly in sets of two, to measure contact forces between the leg and ground along the Y and Z axes, as shown in Fig. 3(c) (normal and tangential to the ground, respectively). The test setup is shown in Fig. 3(d) and the test results are shown in Fig. 4. The beam sample with  $\phi = 90^{\circ}$  was used, and the mass of the foot is represented by a 20 g load attached to the lower left corner of the load frame. The length of the rigid foot is 66.5 mm, and the distance between the translational stage and the plate is  $h = 72 \,\mathrm{mm}$  as shown in Fig. 3(c). Therefore the contact distance between the foot at its unload, natural position and the plate, as depicted by h' in Fig. 3(c) is fixed at 5.5 mm.

Typical trajectories have been selected and plotted in Fig. 4(a). As can be seen, the trajectory evolves as a function of input frequency. In the low-frequency region, where the input frequency is less than 18 Hz, contact interactions dominate the motion observed in the leg, because the "foot" never breaks contact with the ground. This results in trajectories which are a flat line along the Z axis. As the input frequency increases to 26 Hz, ground contact becomes more intermittent and the leg's motion becomes dominated by its own dynamic properties. This results in trajectories that look like a figure '8', or a loop with a single inversion. At the point of contact, the inverted trajectory results in a change in the direction of motion, shown by the orange arrows in Fig. 4(a). At frequencies higher than 38 Hz, the trajectory inverts a second time and the direction of motion at the point of contact reverses again.

The tangential forces measured by the load cells also capture direction changes at the same transition frequencies. In Fig. 4(b), two typical force data are plotted at frequencies of 26 Hz and 40 Hz. By comparing the tangential forces, one can see that the direction is opposite, in line with the change in motion observed in Fig. 4(a). The vertical force data can be used to capture the contact frequency, which is not necessarily the same as the driving frequency. Since contact dominates at frequencies below 18 Hz, we focus on frequencies from 18 Hz to 44 Hz. The result is shown in Fig. 4(c). We highlight three distinct shapes observed with different colors. In each regime, the contact frequency increases with the input frequency. At the transition frequencies noted previously (26 Hz and 38 Hz), the contact frequency drops by  $(\frac{1}{2} \text{ and } \frac{1}{3}, \text{ respectively})$ , the same frequencies at which the foot's trajectory inverts itself and then reverses its direction of motion (and force) on the ground.

It should be noted that this experiment was conducted at a fixed height off the ground. The next section explores how a less-constrained system exhibits similar behavior to produce controllable, walking gaits.

<sup>&</sup>lt;sup>1</sup>Arkema 3DXFLEX<sup>TM</sup> TPE

<sup>&</sup>lt;sup>2</sup>Ultimaker TPU 95A

<sup>&</sup>lt;sup>3</sup>ODrive Dual Shaft Motor D6374 - 150KV

<sup>&</sup>lt;sup>4</sup>Odrive V3.6 High Performance Motor Control.

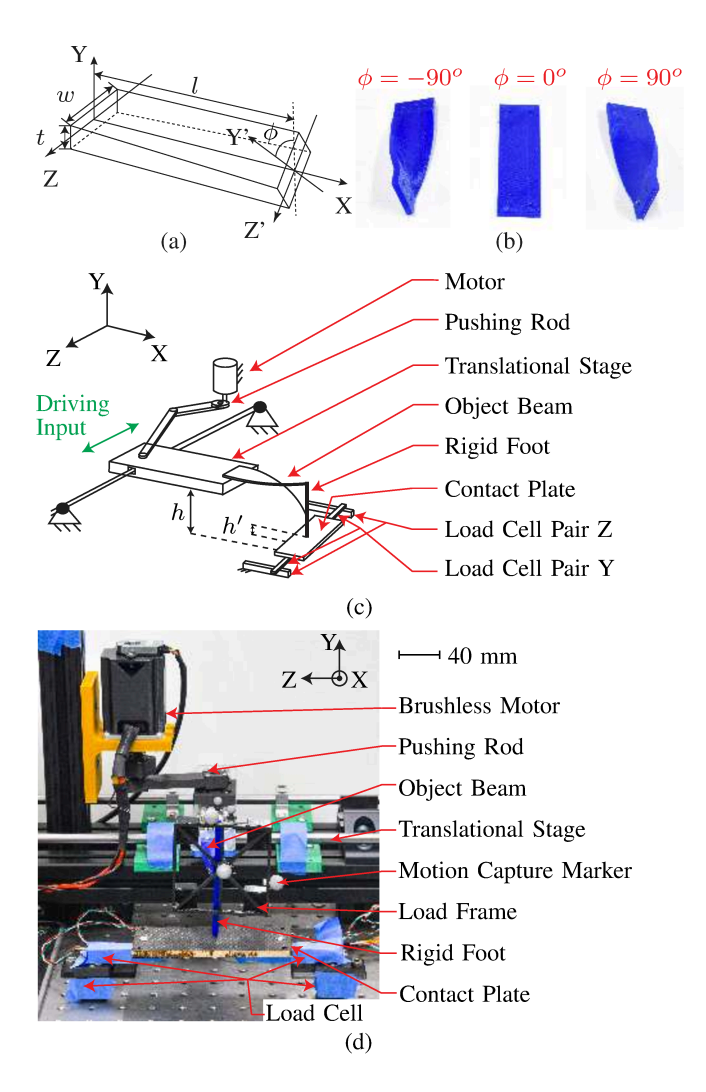


Fig. 3. Lab test setups. (a): Design diagram of the twisted beam. (b): Beam prototype samples. (c): Sketch of lab test setups. (d): Lab test setup for single beam contact tests

# B. Walking Tests

This test demonstrates how the proposed twisted beam can be leveraged to produce a controllable walking gait that can be easily tuned from a single vibrational input.

Two twisted beams serve as robot legs with  $\phi=90^\circ$  and  $\phi=-90^\circ$ , respectively, are mounted in a mirrored fashion across the robot's sagittal plane to a carbon fiber plate. A Maxon brushless motor<sup>5</sup> along with a 40 g offset load is fixed to the plate, serving as a rotary actuation input. The test setup is shown in Fig. 5(a). A vertical slider connects the robot to two translational stages so that the motion of the robot is constrained along the x-axis and about the yaw axis, while the motion about and along the roll, pitch, z-axis, and y-axis is permitted. A cart with a 100 g load is attached to the robot's tail for support and balance. The total length of the walking platform is 295 mm; the total weight is 323 g.

During this test, the motor was commanded to drive the robot at various frequencies from 1 Hz to 80 Hz in 1 Hz

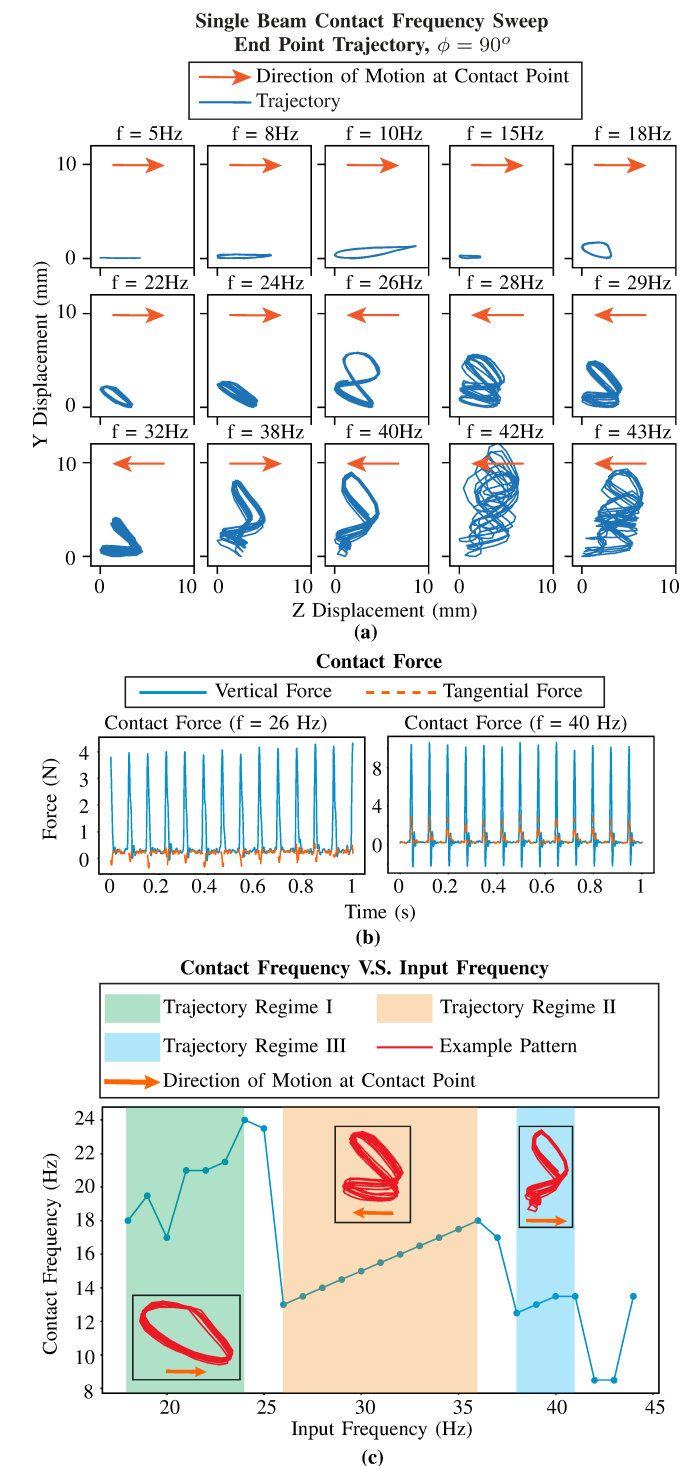


Fig. 4. Results from single beam contact tests. (a): Selected end point trajectories. (b): Contact force data in two directions. (c): Single beam contact test result: contact frequency as a function of the input frequency.

increments. A high-speed camera <sup>6</sup> was used to record the position of the robot at the rate of 1000 fps. Test videos can be found in the supplemental video. Fig. 5(b) presents a cycle of the walking gait at the actuating frequency of 65 Hz. Fig. 5(c) shows the trajectory of the robot in 1 second. In this test,

<sup>&</sup>lt;sup>5</sup>Maxon EC 45 flat Ø42.9 mm, brushless, 30 Watt, with Hall sensors

<sup>&</sup>lt;sup>6</sup>Edgertronic SC1, https://www.edgertronic.com/our-cameras/sc1

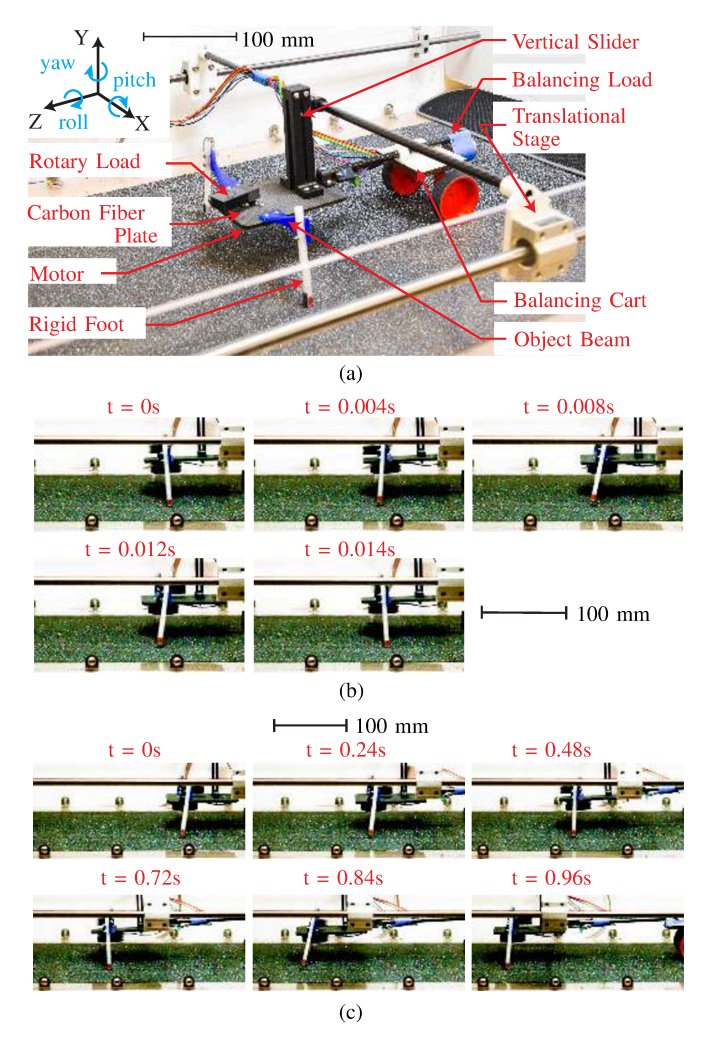


Fig. 5. **Results from walking tests.** (a): Walking test setups. (b): One cycle of walking gait when walking forward. (c): Walking trajectory in 1 sec.

the robot reached the averaged walking speed of 156.3 mm/s with a 65 Hz actuating input frequency. In addition to walking forward, the robot was also able to move backward at a speed of 35.7 mm/s at an input frequency of 23 Hz. The actuation frequencies used for walking forward and backward in these tests differ from the single beam contact test result as shown in Fig. 4(c). This difference can be attributed to 1) Different weight of the driving object, as a single beam is less than 50 g while the walking system is 323 g with two beams; 2) Different contact circumstances, as the timing of two feet contacting the ground can influence each other in as yet unstudied ways; and 3) External friction from the walking test platform. This result demonstrates how foot motion can be tuned by altering a single actuator's input frequency, showing potential for controlling the walking direction and speed of a fully legged terrestrial robot.

#### V. DISCUSSION

Our results demonstrate, through simulation and single beam experiments with contact, that the coupled stiffness of twisted beams can be easily controlled to generate a variety of complex motions by simply changing the beam's input frequency. The results presented above suggest a rich space for control, even from simple actuation sources. These experiments also reveal how highly nonlinear ground contact influences the system's dynamic behavior, which supports the design of walking robots inspired by this phenomenon.

Our experiments progressively move from single beam contact tests to less-constrained studies of system motion with multiple legs in contact with the ground. Through the successive release of constraints, we have demonstrated that the underlying dynamics continue to be influenced by both beam design parameters and input signals. As we continue to release constraints and add legs, we anticipate further challenges with regard to the synchronization of multi-legged systems against the complexity of multiple points of contact vibrating at high speed against the ground. We believe that these topics are outside the scope of the current paper, in which we have primarily focused on the role of design and actuation inputs on single-beam behavior.

Some limitations have also been observed throughout the study. To begin with, we observed that the beam heats up over the course of a long data collection run, which alters material properties such as stiffness and elasticity, impacting results. To address this issue, future designs will integrate materials with lower viscoelastic loss modulus, higher temperature coefficient of Young's modulus, and optimized geometries to reduce shear stresses under vibration, in order to reduce the impact temperature plays on the system's shifting dynamic properties. Another limitation of this work is the lack of a full-body simulation of a multi-legged robot. Simulating our system is challenging because it involves multi-point, soft-body contact with the ground – highly nonlinear interactions that require heavy computation. We plan to employ the newly proposed simplified beam model to simulate the system-level dynamics at faster rates. Once developed, this simulation would permit mechanical design optimization and controller design for understanding the full suite of capabilities in this new legged robot.

## VI. CONCLUSION

In this paper, a mechanism for propagating vibration through soft twisted beams with ground contact is proposed for simplifying the actuation of walking robots by taking advantage of these beams' dynamically-coupled anisotropic stiffness. A simplified model has also been proposed to quickly simulate the nonlinear dynamic behavior of soft twisted beams. Using dynamic simulation and experimental approaches, we have shown that the coupled stiffness of twisted beams with terrain contact can be controlled to generate a variety of complex trajectories by changing the frequency of the input signal. This work also reveals how highly nonlinear ground contact influences the system's dynamic behavior, supporting the design of walking robots inspired by this phenomenon. Future work will explore manufacturing and design strategies for improving consistency between SCRAM elements and minimizing energy loss due to heat. Future work will also include studies on extending the versatility of this concept for locomotion in various media like water and air with gaits like swimming and flapping.

#### **ACKNOWLEDGMENT**

This work is supported by the National Science Foundation Grant No. 1935324.

#### REFERENCES

- N. El-Atab, R. B. Mishra, F. Al-Modaf, L. Joharji, A. A. Alsharif, H. Alamoudi, M. Diaz, N. Qaiser, and M. M. Hussain, "Soft actuators for soft robotic applications: A review," *Advanced Intelligent Systems*, vol. 2, no. 10, p. 2000128, 2020.
- [2] J. Walker, T. Zidek, C. Harbel, S. Yoon, F. S. Strickland, S. Kumar, and M. Shin, "Soft robotics: A review of recent developments of pneumatic soft actuators," *Actuators*, vol. 9, no. 1, 2020.
- [3] S. G. Fitzgerald, G. W. Delaney, and D. Howard, "A review of jamming actuation in soft robotics," *Actuators*, vol. 9, no. 4, pp. 1–31, 2020.
- [4] Y. Jiang, M. Sharifzadeh, and D. M. Aukes, "Reconfigurable soft flexure hinges via pinched tubes," in 2020 IEEE/RSJ International Conference on Intelligent Robots and Systems (IROS), pp. 8843–8850, 2020.
- [5] Y. Jiang, M. Sharifzadeh, and D. M. Aukes, "Shape change propagation through soft curved materials for dynamically-tuned paddling robots," in 2021 IEEE 4th International Conference on Soft Robotics (RoboSoft), pp. 230–237, 2021.
- [6] M. Jiang, Q. Yu, and N. Gravish, "Vacuum induced tube pinching enables reconfigurable flexure joints with controllable bend axis and stiffness," in 2021 IEEE 4th International Conference on Soft Robotics (RoboSoft), pp. 315–320, 2021.
- [7] M. Sharifzadeh and D. M. Aukes, "Curvature-induced buckling for flapping-wing vehicles," *IEEE/ASME Transactions on Mechatronics*, vol. 26, no. 1, pp. 503–514, 2021.
- [8] M. Sharifzadeh, Y. Jiang, and D. M. Aukes, "Reconfigurable curved beams for selectable swimming gaits in an underwater robot," *IEEE Robotics and Automation Letters*, vol. 6, no. 2, pp. 3437–3444, 2021.
- [9] J. D. Watson and F. H. Crick, "Molecular structure of nucleic acids: A structure for deoxyribose nucleic acid," 1974.
- [10] D. Evangelista, S. Hotton, and J. Dumais, "The mechanics of explosive dispersal and self-burial in the seeds of the filaree, erodium cicutarium (geraniaceae)," *Journal of Experimental Biology*, vol. 214, pp. 521–529, 2 2011.
- [11] S. Armon, E. Efrati, R. Kupferman, and E. Sharon, "Geometry and mechanics in the opening of chiral seed pods," *Science*, vol. 333, no. 6050, pp. 1726–1730, 2011.
- [12] H. Gadêlha, P. Hernández-Herrera, F. Montoya, A. Darszon, and G. Corkidi, "Human sperm uses asymmetric and anisotropic flagellar controls to regulate swimming symmetry and cell steering," *Science Advances*, vol. 6, no. 31, p. eaba5168, 2020.
- [13] A. Cardou and C. Jolicoeur, "Mechanical Models of Helical Strands," Applied Mechanics Reviews, vol. 50, pp. 1–14, 01 1997.
- [14] R. L. B. Selinger, J. V. Selinger, A. P. Malanoski, and J. M. Schnur, "Shape selection in chiral self-assembly," *Phys. Rev. Lett.*, vol. 93, p. 158103, Oct 2004.
- [15] R. Ghafouri and R. Bruinsma, "Helicoid to spiral ribbon transition," Physical Review Letters, vol. 94, no. 13, pp. 1–4, 2005.
- [16] M. Wang, B. P. Lin, and H. Yang, "A plant tendril mimic soft actuator with phototunable bending and chiral twisting motion modes," *Nature Communications*, vol. 7, pp. 1–8, 2016.
- [17] M. Cheng and Q. Li, "Left-Handed or Right-Handed? Determinants of the Chirality of Helically Deformable Soft Actuators," *Soft Robotics*, vol. 09, no. 05, pp. 850–860, 2021.
- [18] L. Torsi, G. M. Farinola, F. Marinelli, M. C. Tanese, O. H. Omar, L. Valli, F. Babudri, F. Palmisano, P. G. Zambonin, and F. Naso, "A sensitivity-enhanced field-effect chiralsensor," *Nature Materials*, vol. 7, no. 5, pp. 412–417, 2008.
- [19] Z. Qaiser and S. Johnson, "Generalized spiral spring: A bioinspired tunable stiffness mechanism for linear response with high resolution," *Journal of Mechanisms and Robotics*, vol. 13, no. 1, 2021.
- [20] Y. Yang, K. Vella, and D. P. Holmes, "Grasping with kirigami shells," Science Robotics, vol. 6, no. 54, 2021.
- [21] Z. Zhai, Y. Wang, K. Lin, L. Wu, and H. Jiang, "In situ stiffness manipulation using elegant curved origami," *Science Advances*, vol. 6, no. 47, pp. 1–10, 2020.
- [22] Y. J. Shin, H. J. Lee, K.-S. Kim, and S. Kim, "A robot finger design using a dual-mode twisting mechanism to achieve high-speed motion and large grasping force," *IEEE Transactions on Robotics*, vol. 28, no. 6, pp. 1398–1405, 2012.

- [23] Y. Li, T. Ren, Y. Chen, J. Zhou, Y. Hu, Z. Wang, W. Sun, and C. Xiong, "Untethered multimode fluidic actuation: A new approach to soft and compliant robotics," *Soft Robotics*, vol. 8, no. 1, pp. 71–84, 2021.
- [24] Y. Zhao, Y. Chi, Y. Hong, Y. Li, S. Yang, and J. Yin, "Twisting for soft intelligent autonomous robot in unstructured environments," *Proceedings* of the National Academy of Sciences, vol. 119, no. 22, p. e2200265119, 2022.
- [25] C. Liu and S. M. Felton, "Transformation dynamics in origami," Phys. Rev. Lett., vol. 121, p. 254101, Dec 2018.
- [26] A. T. Baisch, O. Ozcan, B. Goldberg, D. Ithier, and R. J. Wood, "High speed locomotion for a quadrupedal microrobot," *The International Journal of Robotics Research*, vol. 33, no. 8, pp. 1063–1082, 2014.
- [27] C. Karakadıoğlu, M. Askari, and O. Özcan, "The effect of large deflections of joints on foldable miniature robot dynamics," *Journal* of Intelligent and Robotic Systems: Theory and Applications, vol. 100, pp. 15–28, 10 2020.
- [28] A. Maruo, A. Shibata, and M. Higashimori, "Dynamic underactuated manipulator using a flexible body with a structural anisotropy," in 2022 IEEE International Conference on Robotics and Automation (ICRA), 2022.
- [29] J. He and F. Gao, "Mechanism, actuation, perception, and control of highly dynamic multilegged robots: A review," *Chinese Journal of Mechanical Engineering (English Edition)*, vol. 33, 12 2020.
- [30] J. G. Cham, S. A. Bailey, J. E. Clark, R. J. Full, and M. R. Cutkosky, "Fast and robust: Hexapedal robots via shape deposition manufacturing," *The International Journal of Robotics Research*, vol. 21, no. 10-11, pp. 869–882, 2002.
- [31] M. Jiang, Z. Zhou, and N. Gravish, "Flexoskeleton printing enables versatile fabrication of hybrid soft and rigid robots," *Soft Robotics*, vol. 7, no. 6, pp. 770–778, 2020. PMID: 32255734.
- [32] H. H. Hariri, L. A. Prasetya, S. Foong, G. S. Soh, K. N. Otto, and K. L. Wood, "A tether-less legged piezoelectric miniature robot using bounding gait locomotion for bidirectional motion," *Proceedings - IEEE International Conference on Robotics and Automation*, vol. 2016-June, pp. 4743–4749, 2016.
- [33] F. Becker, K. Zimmermann, T. Volkova, and V. T. Minchenya, "An amphibious vibration-driven microrobot with a piezoelectric actuator," *Regular and Chaotic Dynamics*, vol. 18, pp. 63–74, 2013.
- [34] D. Kim, Z. Hao, A. R. Mohazab, and A. Ansari, "On the forward and backward motion of milli-bristlebots," *International Journal of Non-Linear Mechanics*, vol. 127, no. June, p. 103551, 2020.
- [35] T. Li, Z. Zou, G. Mao, X. Yang, Y. Liang, C. Li, S. Qu, Z. Suo, and W. Yang, "Agile and Resilient Insect-Scale Robot," *Soft Robotics*, vol. 6, no. 1, pp. 133–141, 2019.
- [36] A. Tasora, R. Serban, H. Mazhar, A. Pazouki, D. Melanz, J. Fleischmann, M. Taylor, H. Sugiyama, and D. Negrut, "Chrono: An open source multi-physics dynamics engine," in *High Performance Computing in Science and Engineering* (T. Kozubek, R. Blaheta, J. Šístek, M. Rozložník, and M. Čermák, eds.), (Cham), pp. 19–49, Springer International Publishing, 2016.
- [37] S. van der Walt, J. L. Schönberger, J. Nunez-Iglesias, F. Boulogne, J. D. Warner, N. Yager, E. Gouillart, T. Yu, and the scikit-image contributors, "scikit-image: image processing in python," *PeerJ*, vol. 2, p. e453, June 2014
- [38] D. H. Hodges, "A mixed variational formulation based on exact intrinsic equations for dynamics of moving beams," *International Journal of Solids and Structures*, vol. 26, no. 11, pp. 1253–1273, 1990.
- [39] D. H. Hodges, "Geometrically Exact, Intrinsic Theory for Dynamics of Curved and Twisted Anisotropic Beams," *AIAA Journal*, vol. 47, no. 5, pp. 1308–1309, 2009.
- [40] J. R. Banerjee, "Free vibration analysis of a twisted beam using the dynamic stiffness method," *International Journal of Solids and Structures*, vol. 38, no. 38-39, pp. 6703–6722, 2001.
- [41] L. L. Howell and A. Midha, "Parametric deflection approximations for end-loaded, large-deflection beams in compliant mechanisms," *Proceedings of the ASME Design Engineering Technical Conference*, vol. Part F168016-3, no. March 1995, pp. 157–166, 1992.
- [42] L. L. Howell, A. Midha, and T. W. Norton, "Evaluation of equivalent spring stiffness for use in a pseudo-rigid-body model of large-deflection compliant mechanisms," *Journal of Mechanical Design, Transactions of the ASME*, vol. 118, no. 1, pp. 126–131, 1996.
- [43] R. Storn and K. Price, "Differential Evolution A Simple and Efficient Heuristic for global Optimization over Continuous Spaces," *Journal of Global Optimization*, vol. 11, no. 4, pp. 341–359, 1997.
- [44] E. Todorov, T. Erez, and Y. Tassa, "Mujoco: A physics engine for model-based control," in 2012 IEEE/RSJ International Conference on Intelligent Robots and Systems, pp. 5026–5033, 2012.